Electric field tunable superconductor-semiconductor coupling in Majorana nanowires

De Moor, Michiel W.A.; Bommer, Jouri D.S.; Xu, Di; Winkler, Georg W.; Antipov, Andrey E.; Bargerbos, Arno; Wang, Guanzhong; Loo, Nick Van; Op Het Veld, Roy L.M.; Gazibegovic, Sasa

DOI
10.1088/1367-2630/aae61d

Publication date
2018

Document Version
Final published version

Published in
New Journal of Physics

New Journal of Physics
The open access journal at the forefront of physics

Deutsche Physikalische Gesellschaft DPG IOP Institute of Physics

PAPER • OPEN ACCESS

Electric field tunable superconductor-semiconductor coupling in Majorana nanowires

To cite this article: Michiel W A de Moor *et al* 2018 *New J. Phys.* **20** 103049

New Journal of Physics
The open access journal at the forefront of physics

Deutsche Physikalische Gesellschaft DPG
IOP Institute of Physics

Published in partnership with: Deutsche Physikalische Gesellschaft and the Institute of Physics

OPEN ACCESS

RECEIVED
26 June 2018

REVISED
26 August 2018

ACCEPTED FOR PUBLICATION
4 October 2018

PUBLISHED
31 October 2018

PAPER

Electric field tunable superconductor-semiconductor coupling in Majorana nanowires

Michiel W A de Moor[1,7], Jouri D S Bommer[1,7], Di Xu[1,7], Georg W Winkler[2], Andrey E Antipov[2], Arno Bargerbos[1], Guanzhong Wang[1], Nick van Loo[1], Roy L M Op het Veld[1,3], Sasa Gazibegovic[1,3], Diana Car[1,3], John A Logan[4], Mihir Pendharkar[5], Joon Sue Lee[5], Erik P A M Bakkers[1,3], Chris J Palmstrøm[4,5], Roman M Lutchyn[2], Leo P Kouwenhoven[1,6] and Hao Zhang[1,8]

[1] QuTech and Kavli Institute of NanoScience, Delft University of Technology, 2600 GA Delft, The Netherlands
[2] Station Q, Microsoft Research, Santa Barbara, CA 93106-6105, United States of America
[3] Department of Applied Physics, Eindhoven University of Technology, 5600 MB Eindhoven, The Netherlands
[4] Materials Department, University of California, Santa Barbara, CA 93106, United States of America
[5] Electrical and Computer Engineering, University of California, Santa Barbara, CA 93106, United States of America
[6] Microsoft Station Q at Delft University of Technology, 2600 GA Delft, The Netherlands
[7] These authors contributed equally to this work.
[8] Author to whom any correspondence should be addressed.

E-mail: H.Zhang-3@tudelft.nl

Keywords: nanowires, Majorana fermions, superconductivity, spin–orbit coupling

Abstract

We study the effect of external electric fields on superconductor-semiconductor coupling by measuring the electron transport in InSb semiconductor nanowires coupled to an epitaxially grown Al superconductor. We find that the gate voltage induced electric fields can greatly modify the coupling strength, which has consequences for the proximity induced superconducting gap, effective *g*-factor, and spin–orbit coupling, which all play a key role in understanding Majorana physics. We further show that level repulsion due to spin–orbit coupling in a finite size system can lead to seemingly stable zero bias conductance peaks, which mimic the behavior of Majorana zero modes. Our results improve the understanding of realistic Majorana nanowire systems.

1. Introduction

The hybrid superconductor-semiconductor nanowire system is the prime candidate to realize, control, and manipulate Majorana zero modes (MZMs) for topological quantum information processing [1–3]. MZMs can be engineered in these hybrid nanowire systems by combining the one-dimensional nature of the nanowire, strong spin–orbit coupling, superconductivity, and appropriate external electric (to control the chemical potential) and magnetic fields (to control the Zeeman energy) to drive the system into a topologically non-trivial phase [4, 5]. To induce superconductivity in the semiconductor nanowire, it needs to be coupled to a superconductor. The electronic coupling between the two systems turns the nanowire superconducting [6], known as the proximity effect. Following this scheme, the first signatures of MZMs were observed in these hybrid systems, characterized by a zero bias peak (ZBP) in the tunneling conductance spectrum [7–10]. Since then, significant progress has been made in Majorana experiments [11–14], enabled by more uniform coupling between the superconductor and semiconductor nanowire. This has been achieved by improved interface engineering: through careful *ex situ* processing [15–17], by depositing the superconductor on the nanowires *in situ* [18, 19], and a combination of *in situ* and *ex situ* techniques [20], finally leading to the quantization of the Majorana conductance [13].

However, the treatment of the superconductor-semiconductor coupling in the interpretation of experiments is often oversimplified. This coupling has recently been predicted to depend substantially on the confinement induced by external electric fields [21]. In this work, we experimentally show that the superconductor-semiconductor coupling, as parameterized by the induced superconducting gap, is affected by

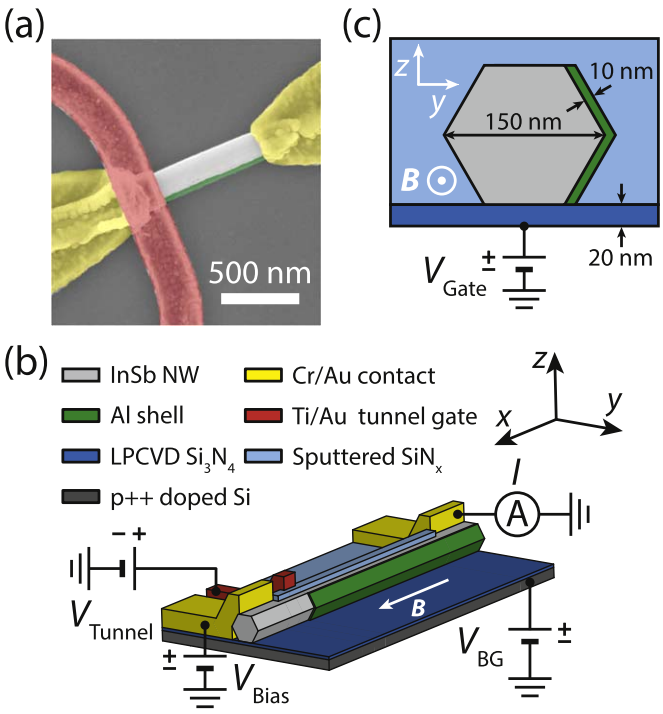

Figure 1. Device schematics. (a) SEM of device A, with InSb nanowire in gray, superconducting aluminum shell in green, Cr/Au contacts in yellow, and local tunnel gate in red. Scale bar is 500 nm. (b) Schematic of experimental set-up. The substrate acts as a global back gate. The magnetic field is applied along the nanowire direction (x-axis). (c) Geometry used in the numerical simulations. A uniform potential V_{Gate} is applied as a boundary condition at the interface between substrate and dielectric. The superconductor (green) is kept at a fixed potential, which is set by the work function difference at the superconductor-semiconductor interface.

gate induced electric fields. Due to the change in coupling, the renormalization of material parameters is altered, as evidenced by a change in the effective g-factor of the hybrid system. Furthermore, the electric field is shown to affect the spin–orbit interaction, revealed by a change in the level repulsion between Andreev states. Our experimental findings are corroborated by numerical simulations.

2. Experimental set-up

We have performed tunneling spectroscopy experiments on four InSb–Al hybrid nanowire devices, labeled A–D, all showing consistent behavior. The nanowire growth procedure is described in [20]. A scanning electron micrograph (SEM) of device A is shown in figure 1(a). Figure 1(b) shows a schematic of this device and the measurement set-up. For clarity, the wrap-around tunnel gate, tunnel gate dielectric and contacts have been removed on one side. A normal-superconductor (NS) junction is formed between the part of the nanowire covered by a thin shell of aluminum (10 nm thick, indicated in green, S), and the Cr/Au contact (yellow, N). The transmission of the junction is controlled by applying a voltage V_{Tunnel} to the tunnel gate (red), galvanically isolated from the nanowire by 35 nm of sputtered SiN_x dielectric. The electric field is induced by a global back gate voltage V_{BG}, except in the case of device B, where this role is played by the side gate voltage V_{SG}. Further details on device fabrication and design are included in appendices A and B. To obtain information about the density of states (DOS) in the proximitized nanowire, we measure the differential conductance $\mathrm{d}I/\mathrm{d}V_{\mathrm{Bias}}$ as a function of applied bias voltage V_{Bias}. In the following, we will label this quantity as $\mathrm{d}I/\mathrm{d}V$ for brevity. A magnetic field is applied along the nanowire direction (x-axis in figures 1(b), (c)). All measurements are performed in a dilution refrigerator with a base temperature of 20 mK.

3. Theoretical model

The device geometry used in the simulation is shown in figure 1(c). We consider a nanowire oriented along the x-direction, with a hexagonal cross-section in the yz-plane. The hybrid superconductor-nanowire system is described by the Bogoliubov–de Gennes (BdG) Hamiltonian

$$H = \left[\frac{\hbar^2\mathbf{k}^2}{2m^*} - \mu - e\phi\right]\tau_z + \alpha_y(k_z\sigma_x - k_x\sigma_z)\tau_z + \alpha_z(k_x\sigma_y - k_y\sigma_x)\tau_z + \frac{1}{2}g\mu_B B\sigma_x + \Delta\tau_x. \quad (1)$$

The first term contains contributions from the kinetic energy and the chemical potential, as well as the electrostatic potential ϕ. The second and third terms describe the Rashba spin–orbit coupling, with the coupling strength α_y (α_z) depending on the y-component (z-component) of the electric field. The Zeeman energy contribution, proportional to g, the Landé g-factor, is given by the fourth term. Finally, the superconducting pairing Δ is included as the fifth term. All material parameters are position dependent, taking different values in the InSb nanowire and the Al superconductor. For additional details about the simulation, see appendices C and D.

If the coupling between the superconductor and semiconductor is small (compared to the bulk gap of the superconductor Δ, known as weak coupling), superconductivity can be treated as a constant pairing potential term in the nanowire Hamiltonian, with the induced superconducting gap being proportional to the coupling strength [22]. However, if the coupling becomes strong, the wave functions of the two materials hybridize, and the superconductor and semiconductor have to be considered on equal footing [23]. We achieve this by solving the Schrödinger equation in both materials simultaneously. When desired, the orbital effect of the magnetic field is added via Peierls substitution [24]. The simulations are performed using the `kwant` package [25].

The electrostatic potential in the nanowire cross-section is calculated from the Poisson equation, assuming an infinitely long wire. We use a fixed potential V_{Gate} as a boundary condition at the dielectric-substrate interface. The superconductor enters as the second boundary condition, with a fixed potential to account for the work function difference between superconductor and semiconductor [26]. We approximate the mobile charges in the nanowire by a 3D electron gas (Thomas–Fermi approximation). It has been demonstrated that the potentials calculated using this approximation give good agreement with results obtained by self-consistent Schrödinger–Poisson simulations [27]. The calculated potential for a given V_{Gate} is then inserted into the Hamiltonian (1).

By solving the Schrödinger equation for a given electrostatic environment, we can see how the gate potential alters the electronic states in the nanowire, how they are coupled to the superconductor, and how this coupling affects parameters such as the induced gap, effective g-factor, and spin–orbit energy.

4. Gate voltage dependence of the induced superconducting gap

When the transmission of the NS-junction is sufficiently low (i.e., in the tunneling regime), the differential conductance $\mathrm{d}I/\mathrm{d}V$ is a direct measure of the DOS in the proximitized nanowire [28]. In figure 2(a), we plot $\mathrm{d}I/\mathrm{d}V$ measured in device A as a function of applied bias voltage V_{Bias} and tunnel gate voltage V_{Tunnel}, for $V_{\text{BG}} = -0.6$ V. In the low transmission regime, we resolve the superconducting gap Δ around 250 μeV, indicated by the position of the coherence peaks. The ratio of sub-gap to above-gap conductance (proportional to the normal state transmission of the junction, T) follows the behavior expected from BTK theory [29, 30], indicating the sub-gap conductance is dominated by Andreev reflection processes (proportional to T^2). This is generally referred to as a hard gap. However, for more positive back gate voltages, the sub-gap conductance is larger and shows more resonances, as is illustrated in figure 2(b) for $V_{\text{BG}} = -0.3$ V. Figure 2(c) shows line traces taken at a similar transmission (above-gap conductance) for both cases. The sub-gap conductance for $V_{\text{BG}} = -0.3$ V (black line) exceeds that of the hard gap case (red line) by an order of magnitude. This is indicative of a surplus of quasi-particle states inside the gap, referred to as a soft gap.

The gate voltage induced transition from soft to hard gap is generically observed in multiple devices. To understand this phenomenology, we calculate the electron density in the nanowire cross-section for different values of V_{Gate}. Because the charge neutrality point in our devices is unknown, there is a difference between the gate voltages used in the experiment and the values of V_{Gate} used in the simulation. By comparing the transition point between hard and soft gaps in the experiment and the simulation, we estimate that the experimental gate voltage range $-0.6\text{ V} < V_{\text{BG}} < -0.4$ V roughly corresponds to the simulated gate voltage range $-0.4\text{ V} < V_{\text{Gate}} < -0.2$ V.

For more negative V_{Gate}, the electric field from the gate pushes the electrons towards interface with the superconductor (inset of figure 2(a)). We solve the Schrödinger equation for the calculated electrostatic potential and find that this stronger confinement near the interface leads to a stronger coupling. This results in a hard gap, as illustrated by the calculated energy spectrum (figure 2(d), red line). However, for more positive voltages, the electrons are attracted to the back gate, creating a high density pocket far away from the superconductor (inset of figure 2(b)). These states are weakly coupled to the superconductor, as demonstrated

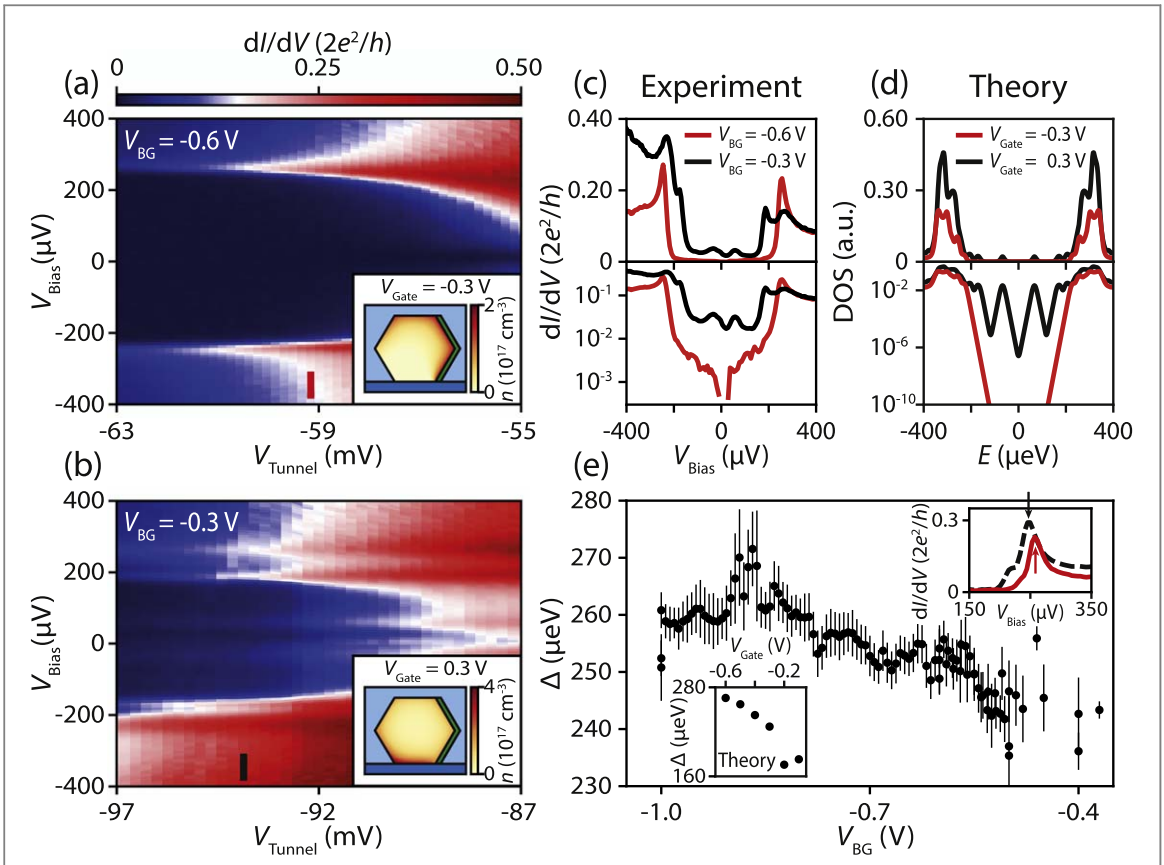

Figure 2. Gate dependence of the induced superconducting gap. (a), (b) Differential conductance dI/dV measured in device A as a function of V_{Bias} and V_{Tunnel} for $V_{\mathrm{BG}} = -0.6$ V (a) and $V_{\mathrm{BG}} = -0.3$ V (b). Insets show the calculated electron density in the wire for $V_{\mathrm{Gate}} = -0.3$ V and $V_{\mathrm{Gate}} = 0.3$ V, respectively. (c) Line-cuts from (a) and (b), indicated by the colored bars, in linear (top) and logarithmic (bottom) scale. (d) Calculated DOS for the density profiles shown in the insets of (a) and (b), shown in red and black, respectively. (e) Induced gap magnitude Δ as a function of V_{BG}, showing a decrease for more positive gate voltages. Top right inset: line traces showing the coherence peak position (indicated by the arrow) for $V_{\mathrm{BG}} = -0.6$ V (solid red line) and $V_{\mathrm{BG}} = -0.4$ V (dashed black line). Bottom left inset: induced gap from the calculated DOS as a function of V_{Gate}, consistent with the experimental observation.

by a soft gap structure (figure 2(d), black line, see also appendix E). We can therefore conclude that the electron tunneling between the semiconductor and the superconductor is strongly affected by the gate potential.

The change in superconductor-semiconductor coupling does not just affect the hardness, but also the size of the gap. For each back gate voltage, we fit the BCS-Dynes expression [31] for the DOS in order to extract the position of the coherence peaks, giving the gap size Δ. The results are shown in figure 2(e). Further details on the fitting procedure are given in appendix F. As V_{BG} becomes more positive, the superconductor-semiconductor coupling becomes weaker, reducing the size of the gap. From $V_{\mathrm{BG}} > -0.4$ V onward it becomes difficult to accurately determine the gap, as it tends to become too soft and the coherence peaks are not always clearly distinguishable. The top right inset shows the shift of the coherence peak (indicated by the arrows) to lower bias voltage as V_{BG} is increased. The lower left inset shows the extracted coherence peak position from the numerical simulations, showing the same trend with gate voltage. However, the theoretically calculated induced gap is generally smaller than the experimentally observed gap. It has been demonstrated that disorder at the outer surface of the superconductor (e.g., due to oxidation) leads to an increase in the induced gap due to breaking of momentum conservation, which increases the superconductor-semiconductor hybridization [21]. Additionally, the gap decreases more slowly when the gate voltage is more positive. As this kind of disorder is present in our devices, but was not included in the simulation, this is a likely cause for the discrepancy between theory and experiment.

5. Effective *g*-factor

As the electric field induced by the back gate clearly has an important effect on the hybridization between the nanowire and the superconductor, we now look at the effect this has on the Zeeman term in the Hamiltonian. This term affects the energy dispersion of spinful states in a magnetic field. We study the dispersion of the states in the nanowire by measuring dI/dV in device A as a function of applied bias voltage and magnetic field, as

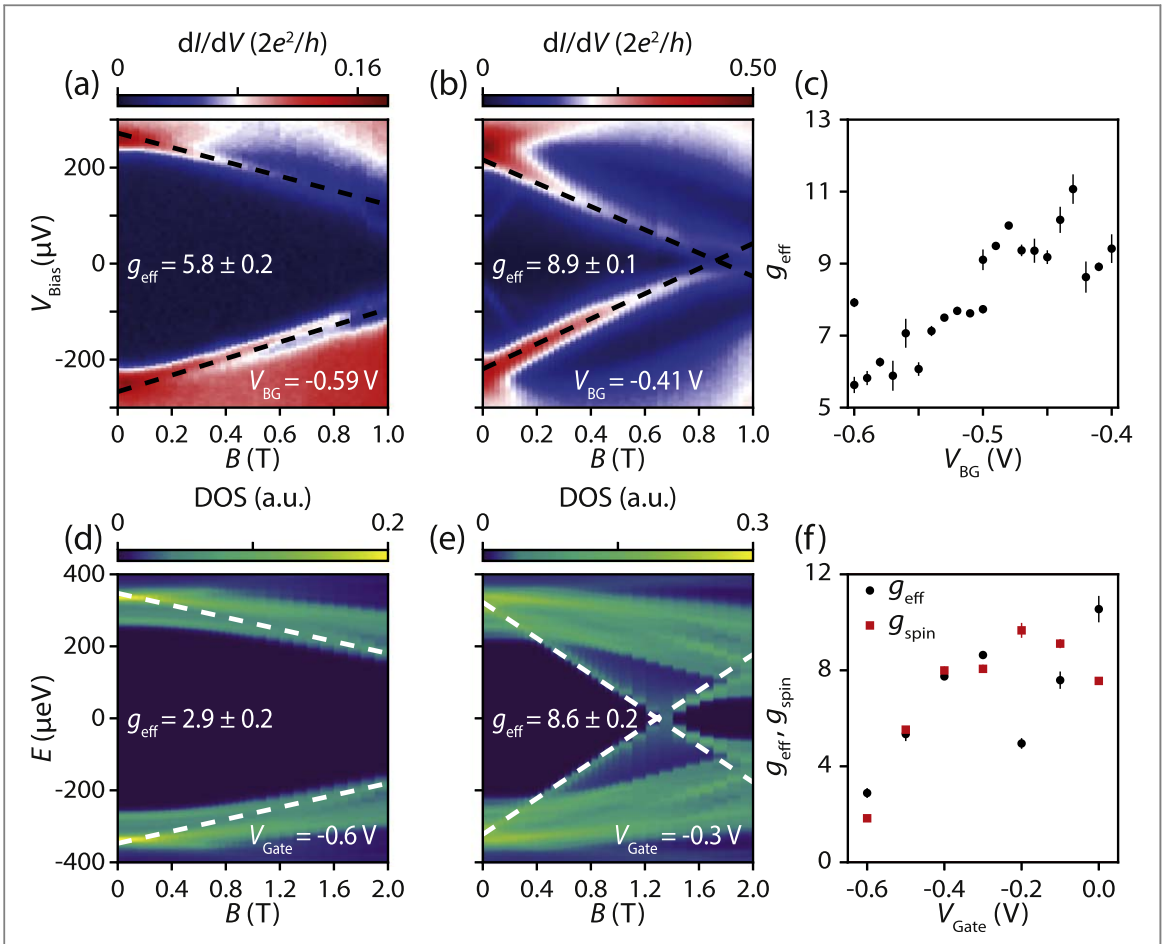

Figure 3. Effective g-factor. (a), (b) $\mathrm{d}I/\mathrm{d}V$ measured in device A as a function of applied bias voltage V_{Bias} and magnetic field B for $V_{\mathrm{BG}} = -0.59$ V and $V_{\mathrm{BG}} = -0.41$ V, respectively. The effective g-factor is extracted from a linear fit of the lowest energy state dispersion (dashed lines). (c) g_{eff} as a function of V_{BG}, showing an increase as the gate voltage becomes more positive. Data from device A. (d), (e) Simulated DOS in the nanowire as a function of magnetic field for $V_{\mathrm{Gate}} = -0.6$ V and $V_{\mathrm{Gate}} = -0.3$ V, respectively. (f) Extracted g_{eff} (based on lowest energy state in the spectrum, black circles) and g_{spin} (based on the spectrum at $k = 0$, red squares) from the simulation.

shown in figures 3(a) and (b). We define the effective g-factor as $g_{\mathrm{eff}} = \frac{2}{\mu_{\mathrm{B}}}\left|\frac{\Delta E}{\Delta B}\right|$, with $\left|\frac{\Delta E}{\Delta B}\right|$ the absolute value of the average slope of the observed peak in the differential conductance as it disperses in magnetic field. This effective g-factor is different from the pure spin g-factor g_{spin}, as the dispersion used to estimate g_{eff} is generally not purely linear in magnetic field, and has additional contributions from the spin–orbit coupling, magnetic field induced changes in chemical potential, and orbital effects [21, 26, 32]. The effective g-factor is the parameter which determines the critical magnetic field required to drive the system through the topological phase transition [33]. We obtain the slope $\frac{\Delta E}{\Delta B}$ from a linear fit (shown as black dashed lines in figures 3(a), (b), see appendix G for details) of the observed peak position. Figure 3(c) shows the extracted g_{eff} for device A, with more positive back gate voltages leading to larger g_{eff} (visible as a steeper slope). A similar result has recently been reported in hybrid InAs–Al nanowires [34].

We use our numerical model to calculate the DOS in the nanowire as a function of applied magnetic field, shown in figures 3(d) and (e). From the calculated spectrum, we apply the same procedure used to fit the experimental data to extract g_{eff} (white dashed lines). The results for different values of V_{Gate} are given in figure 3(f) as black circles. The applied back gate voltage changes the hybridization of the states in the InSb ($|g_{\mathrm{spin}}| = 40$ [35]) and the Al ($|g_{\mathrm{spin}}| = 2$). As a more positive gate voltage increases the weight of the wave function in the InSb, we expect the renormalized g-factor to increase as the gate voltage is increased, consistent with the results of figures 3(c) and (f).

To see how well g_{eff} describes the Zeeman term in the Hamiltonian, we turn our attention to the energy spectrum at $k = 0$. At this point, the effect of spin–orbit coupling vanishes. If orbital effects are excluded, we can then define the absolute value of the pure spin g-factor as $g_{\mathrm{spin}} = \frac{2}{\mu_{\mathrm{B}}}\left|\frac{\Delta E(k=0)}{\Delta B}\right|$. The resulting values for g_{spin} are shown as red squares in figure 3(f). By comparing the results for g_{eff} and g_{spin}, we can conclude that when the lowest energy state has a momentum near $k = 0$ (as is the case for $V_{\mathrm{Gate}} < -0.2$ V), the effect of spin–orbit

coupling is negligible, and $g_{\rm eff}$ is a good proxy for the pure spin g-factor. However, when this is no longer the case, deviations can be observed, as is the case for $V_{\rm Gate} \geqslant -0.2$ V. As we expect the experimental gate voltage range of figure 3(c) to be comparable to values of $V_{\rm Gate} < -0.2$ V, we conclude that the experimentally obtained $g_{\rm eff}$ is a reasonable approximation of $g_{\rm spin}$ in this parameter regime. However, we stress once more that in general, one needs to be careful when interpreting the $g_{\rm eff}$ extracted from experimental data as the g-factor entering the Hamiltonian in the Zeeman term.

The increasing trend of $g_{\rm eff}$ does not change when the orbital effect of magnetic field is considered (see appendix G, figure G4). However, there is a significant increase in the predicted values, in agreement with previous findings for InAs nanowires [32]. The values in figure G4 are larger than the ones generally observed in our experiment (see figure 3(c)), suggesting that the orbital effect is not a dominant mechanism in determining the effective g-factor in these devices. We note that the data from device A used to make these plots was taken solely in the hard gap regime, where one expects a strong confinement near the superconductor. This suppresses the orbital contribution of the magnetic field. Another possible explanation for the discrepancy between the results of the simulation and the experimental data is an overestimation of the density in the nanowire, as higher sub-bands have a stronger contribution from the orbital effect. Minimizing the orbital effect is desirable for Majorana physics, as the orbital contributions of the magnetic field are detrimental to the topological gap [24].

6. Level repulsion due to spin–orbit coupling

The term in the Hamiltonian that remains to be explored describes the Rashba spin–orbit coupling. The strength of the spin–orbit coupling is determined by the parameter α, which depends on the material (and thus, on the superconductor-semiconductor coupling), and the electric field [36–38]. Therefore, we expect that this term will be affected by the gate potential as well. In finite systems, the spin–orbit interaction can couple states with different orbitals and spins [39]. These states are thus no longer orthogonal to each other, and the spin–orbit mediated overlap between them causes energy splitting, leading to level repulsion [40–42]. This level repulsion, which is generic in class D systems in the presence of superconductivity, magnetic field and spin–orbit coupling [43, 44], can be extracted from the low energy nanowire spectrum as measured by tunneling spectroscopy [45].

In figures 4(a)–(c), we show the evolution of the level repulsion between the two lowest energy sub-gap states (labeled L_1 and L_2, as indicated by the white dashed lines in panel (c)) in device B. For these measurements, the global back gate is grounded, with the electric field being induced by applying a voltage to the side gate (side gate shown in appendix B).

We parameterize the level repulsion by two quantities: the coupling strength $\delta_{\rm SO}$, and the splitting A, defined as the maximum deviation of L_1 from zero energy after the first zero crossing. This splitting has previously been linked to the overlap between two MZM in a finite system [46]. In figure 4(e), we zoom in on the anti-crossing feature in panel figure 4(b), showing the minimum energy difference between L_1 and L_2 (given by $2\delta_{\rm SO}$) and the splitting A. We extract these parameters by a fit of the anti-crossing (solid green lines, with the uncoupled states shown by the dashed black lines, details of the fitting procedure are in appendix H).

Because we expect finite size effects to be relevant, we cannot use our previous theoretical model, as it is based on an infinitely long nanowire. Therefore, we modify the model to take into account the finite size of the nanowire system, and calculate the low energy spectrum for different values of the Rashba spin–orbit strength (see appendix I). In figure 4(d), we plot the two lowest energy states in the nanowire as a function of the Zeeman energy ($E_{\rm Z} = \frac{1}{2} g \mu_{\rm B} B$), in units of the superconducting gap Δ. If $\alpha = 0$ (no spin–orbit coupling, dashed black lines), there is no coupling between the states, and no level repulsion occurs. However, if spin–orbit coupling is included (e.g., $\alpha = 0.1$ eV Å, solid red lines), the levels repel each other, with the magnitude of the anti-crossing given by 2δ. The level repulsion strength scales with α (inset of figure 4(d)), providing a way to estimate α based on the low energy spectrum using $2\delta \sim \alpha\pi/l$, where l is the length of the nanowire.

In figure 4(f), we plot $\delta_{\rm SO}$ (black circles) and A (red squares) as a function of the applied side gate voltage. The two parameters follow opposite trends, with A being maximal when $\delta_{\rm SO}$ is minimal. When $\delta_{\rm SO}$ is larger, the levels repel each other more, leading to L_1 being pushed closer to zero energy, reducing the splitting A. When $V_{\rm SG} < 2.0$ V, both parameters become smaller with decreasing $V_{\rm SG}$. At this point, other states at higher energies become relevant for the lowest energy dispersion (a situation demonstrated in figure 4(a)), and our method to extract these parameters breaks down. We expect this method to be reliable when the energetically lowest two states can be clearly separated from the rest.

Because $\delta_{\rm SO}$ depends not only on α, but also on the details of the confinement potential, as well as the coupling to the superconductor, a precise estimate goes beyond the current approximations in our model. That being said, based on the observed magnitude of $\delta_{\rm SO}$ and our simulations of the finite nanowire system, we can

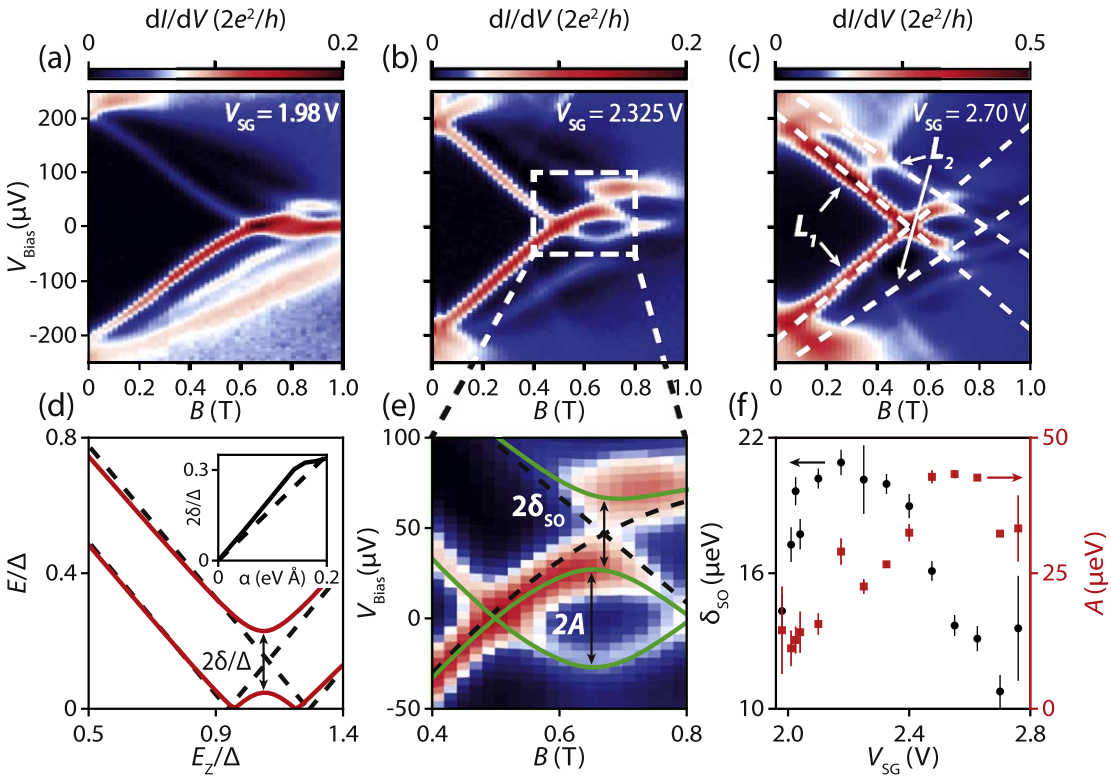

Figure 4. Spin–orbit coupling induced level repulsion. (a)–(c) dI/dV as a function of V_{Bias} for device B, showing the dispersion of subgap states in magnetic field, for $V_{SG} = 1.98$ V, 2.325 V, and 2.70 V, respectively. The two lowest energy states L_1, L_2, and their particle–hole symmetric partners are indicated by the white dashed lines. (d) Calculated low energy spectrum of the finite nanowire system as a function of the Zeeman energy E_Z for $\alpha = 0$ eV Å (dashed black lines) and $\alpha = 0.1$ eV Å (solid red lines), showing the opening of an energy gap 2δ due to spin–orbit coupling. Inset: the energy gap 2δ as a function of the Rashba α parameter (solid line), and the estimate $2\delta = \alpha\pi/l$ (dashed line), with l the nanowire length. All energy scales are in units of the superconducting gap Δ. (e) Zoom-in of the anti-crossing in (b), showing the splitting A and the coupling strength δ_{SO}. Green solid lines indicate a fit of the anti-crossing, with the dashed black lines showing the uncoupled energy levels. (f) Coupling δ_{SO} (black circles) and splitting A (red squares) as a function of V_{SG}, showing opposite trends for these parameters.

estimate the Rashba parameter α to be around 0.1 eV Å in this gate voltage range. This value is comparable to the values reported in InSb nanowire based quantum dots [47], and smaller than the values measured in weak anti-localization experiments [37]. A large value of α is beneficial for Majorana physics, as it determines the maximum size of the topological gap [48].

7. ZBP in extended magnetic field range

In the previous sections, we have described the effect of the gate induced electric field on the various terms in the Hamiltonian (1). As this Hamiltonian is known to describe Majorana physics, we now turn our attention to possible signatures of MZMs in this system. In particular, when $2\delta_{SO}$ becomes comparable to the energy of L_2, we find that L_1 can become pinned close to zero bias over an extended range in magnetic field, as demonstrated in figure 5(b) (data from device A). Figure 5(d) shows that the state stays pinned to zero energy over a range of over 0.2 T, corresponding to a Zeeman energy of over 300 μeV, which is larger than the induced gap. The stability of the ZBP in terms of the ratio of Zeeman energy to induced gap is comparable to the most stable ZBPs reported in literature [11, 12]. When we fix the magnetic field to $B = 0.26$ T and change the back gate voltage (figure 5(e)), it appears that there is a stable ZBP over a few mV as well.

We might be tempted to conclude that this stability implies this is a MZM. However, if we change either the gate voltage (figures 5(a), (c)) or the magnetic field (figure 5(f)) a little bit, we observe that this stability applies only to very particular combinations of gate voltage and magnetic field. One should keep in mind that in a finite system, MZMs are not expected to be stable with respect to local perturbations if the system size is comparable to the Majorana coherence length, which is likely the case in our devices. This further complicates the determination of the origin of the observed peaks. As we find no extended region of stability, we conclude that it is unlikely that this state pinned to zero energy is caused by a topological phase transition. Rather, this seems to be due to a fine-tuned coincidence in which the repulsion between two states combined with particle–hole

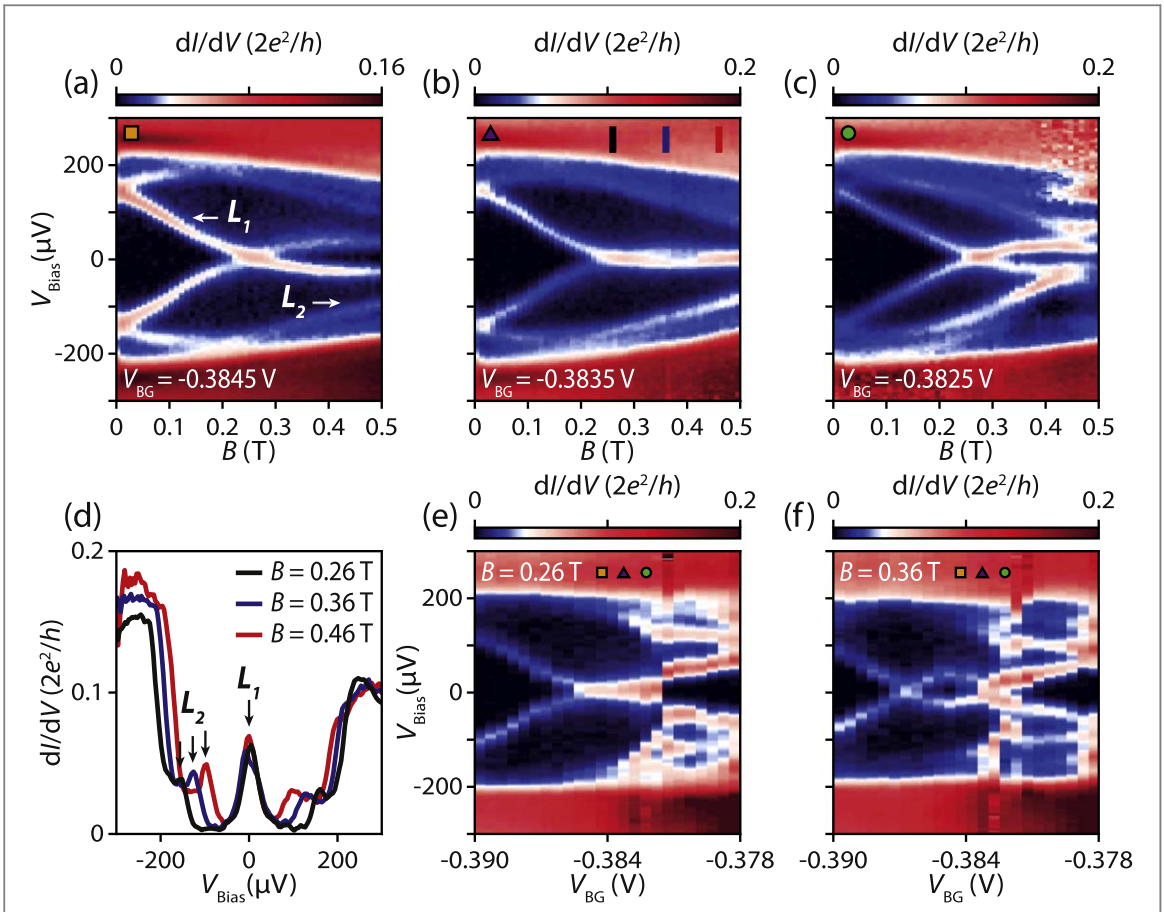

Figure 5. Zero bias pinning due to strong level repulsion. (a)–(c) $\mathrm{d}I/\mathrm{d}V$ as a function of V_{Bias} for device A, showing the dispersion of L_1 and L_2 as a function of magnetic field for $V_{\mathrm{BG}} = -0.384$ 5V, -0.383 5V, and -0.382 5V, respectively. (d) Line traces at magnetic fields indicated by the colored bars in (b), showing the stable pinning of L_1 to zero bias voltage. (e), (f) $\mathrm{d}I/\mathrm{d}V$ measured as a function of V_{BG} at fixed magnetic field $B = 0.26$ T and 0.36 T, respectively. Gate voltages from (a)–(c) are indicated by orange square, purple triangle, and green circle, respectively.

symmetry leads to one of the states being pinned to $E = 0$. We reiterate that simply having a stable zero energy state over an extended range in magnetic field is not sufficient to make claims about robust Majorana modes [49–51]. Further experimental checks, such as stability of the ZBP in an extended region of the parameter space spanned by the relevant gate voltages [11], as well as magnetic field, are required in order to assign a possible Majorana origin.

8. Conclusion and outlook

We have used InSb nanowires with epitaxial Al superconductor to investigate the effect of the gate voltage induced electric field on the superconductor-semiconductor coupling. This coupling is determined by the distribution of the wave function over the superconductor and semiconductor, and controls essential parameters of the Majorana Hamiltonian: the proximity induced superconducting gap, the effective g-factor, and spin–orbit coupling. Our observations show that the induced superconductivity, as parameterized by the hardness and size of the induced gap, is stronger when the electrons are confined to a region close to the superconductor. The stronger coupling leads to a lower effective g-factor. We also determine that the gate voltage dependence of the effective g-factor is dominated by the change in coupling to the superconductor, rather than by orbital effects of the magnetic field. Finally, we study the effect of level repulsion due to spin–orbit coupling. Appropriate tuning of the repulsion leads to level pinning to zero energy over extended parameter ranges, mimicking the behavior expected from MZMs. Our result deepens the understanding of a more realistic Majorana nanowire system. More importantly, it is relevant for the design and optimization of future advanced nanowire systems for topological quantum information applications.

Acknowledgments

We thank JG Kroll, A Proutski, and S Goswami for useful discussions. This work has been supported by the European Research Council, the Dutch Organization for Scientific Research, the Office of Naval Research, the Laboratory for Physical Sciences, and Microsoft Corporation Station Q.

Author contributions

MWAdM, JDSB, DX, and HZ fabricated the devices, performed the measurements, and analyzed the data. GWW, AB, AEA, and RML performed the numerical simulations. NvL and GW contributed to the device fabrication. RLMOhV, SG, and DC grew the InSb nanowires under the supervision of EPAMB. JAL, MP, and JSL deposited the aluminum shell on the nanowires under the supervision of CJP. LPK and HZ supervised the project. MWAdM and HZ wrote the manuscript with comments from all authors. MWAdM, JDSB, and DX contributed equally to this work.

Appendix A. Fabrication procedure

1. *Nanowire deposition*: a SEM-based nanomanipulator is used to deterministically place the InSb–Al nanowires unto a degenerately p-doped Si substrate covered by 20 nm of LPCVD Si_3N_4 (devices A, C, and D) or 285 nm of thermal SiO_2 (device B).
2. *Mask preparation and lithography*: for every fabrication step, we use standard electron beam lithography techniques to create the mask. The mask consists of a layer of PMMA 950KA6 spun at 4000 rpm. After writing, the mask is developed in a solution of MIBK:IPA (1:3 ratio) for 60 s, followed by a IPA rinse for 60 s. After each deposition step, liftoff is done using acetone.
3. *Contact preparation and deposition*: before depositing the contact material, the Al and AlO_x are locally removed by Ar plasma etch. The contacts are deposited by electron beam evaporation of Cr/Au (10/100-200 nm). For device B, the side gates are also evaporated in this step.
4. *Dielectric deposition*: as a top gate dielectric we sputter 35 nm of SiN_x (devices A, C, and D).
5. *Top gate deposition*: the top gates are deposited by electron beam evaporation of Ti/Au (10/200 nm) (devices A, C, and D).

Appendix B. Device information and schematics

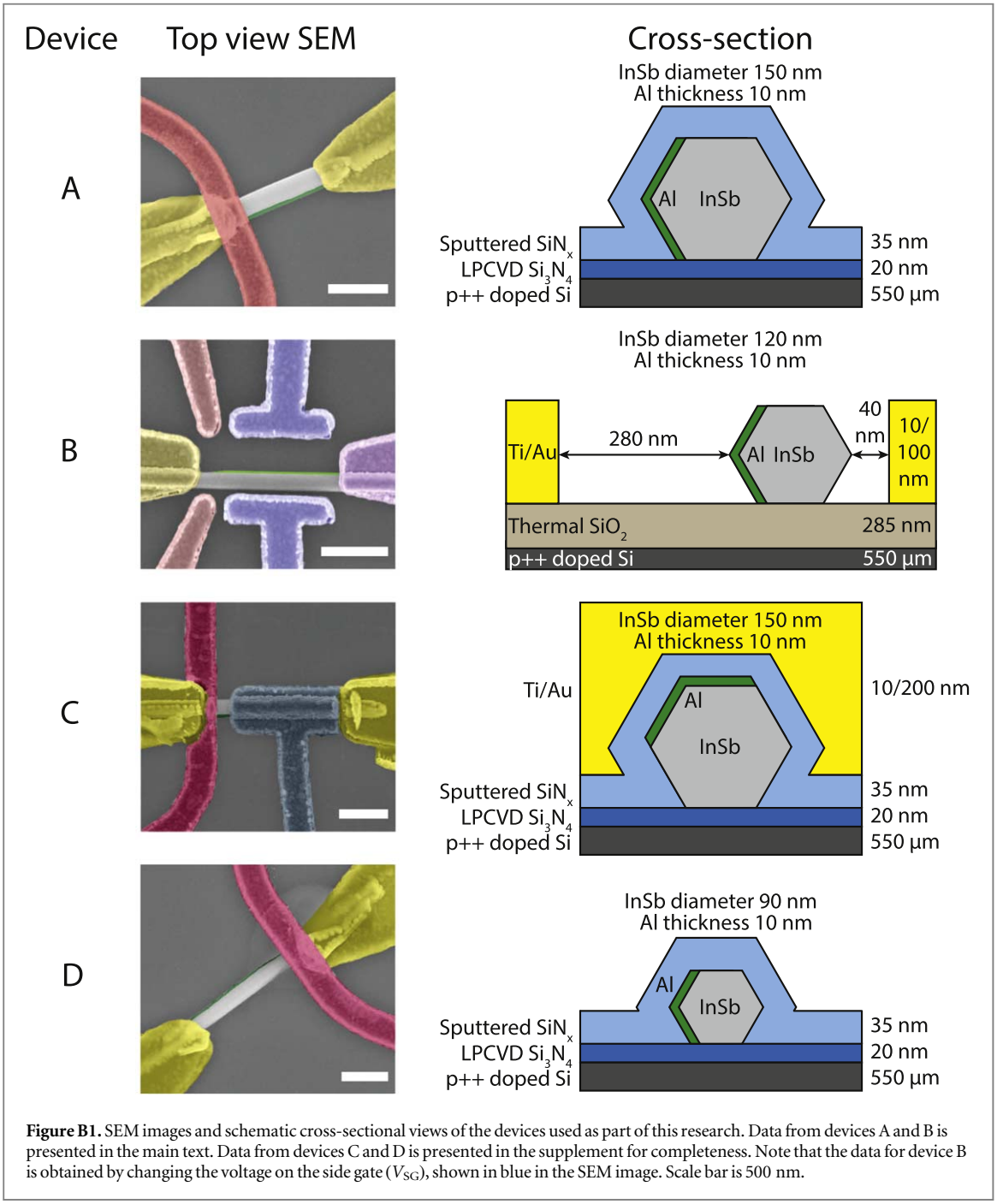

Figure B1. SEM images and schematic cross-sectional views of the devices used as part of this research. Data from devices A and B is presented in the main text. Data from devices C and D is presented in the supplement for completeness. Note that the data for device B is obtained by changing the voltage on the side gate (V_{SG}), shown in blue in the SEM image. Scale bar is 500 nm.

Appendix C. Simulation of electrostatics and nanowire spectrum

For the electrostatics simulations we use the geometry of device A (as shown in figure 1(c) of the main text). We describe the device as an infinite wire oriented along the x-direction, with a hexagonal cross-section in the yz-plane. The electrostatics are described by the Poisson equation

$$\nabla \cdot (\epsilon_r(\mathbf{r})\nabla\phi(\mathbf{r})) = \frac{\rho_{\text{tot}}[\phi(\mathbf{r})]}{\epsilon_0}, \tag{C.1}$$

where $\rho_{\text{tot}}[\phi(\mathbf{r})]$ is a functional of the potential $\phi(\mathbf{r})$. We include four contributions to ρ_{tot},

$$\rho_{\text{tot}} = \rho_{\text{e}} + \rho_{\text{hh}} + \rho_{\text{lh}} + \rho_{\text{fixed}}, \tag{C.2}$$

where ρ_{e}, ρ_{hh} and ρ_{lh} are the mobile charges of the conduction band, heavy hole (hh) band and light hole (lh) band of the InSb nanowire and ρ_{fixed} are the fixed charges in the system. For the mobile electron charges we assume a 3D electron gas density (Thomas–Fermi approximation)

Table C1. Material parameters for InSb and Al.

Parameter	InSb	Al
m^*	0.013 9 [52]	1
g	−40 [35]	2
Δ	0 meV	0.34 meV [54]
E_F	0 eV	10 eV [55]

$$\rho_e(\phi) = -\frac{e}{3\pi^2}\left(\frac{2m_e|\phi|\theta(-\phi)}{\hbar^2}\right)^{3/2}, \tag{C.3}$$

with θ the Heaviside step function, and for the holes

$$\rho_i(\phi) = \frac{e}{3\pi^2}\left(\frac{2m_i|\phi - E_G|\theta(\phi - E_G)}{\hbar^2}\right)^{3/2}, \tag{C.4}$$

with E_G the band gap and i corresponding to the hh and lh band, respectively. For the effective masses, we take the bulk InSb values [52]. We include hole bands to describe the additional screening when the electrochemical potential is in the valence band, which can become relevant for very negative gate voltages due to the narrow band gap of InSb. To model the influence of the sputtered dielectric on the nanowire surface, the wire is wrapped in a 1nm surface layer of 2.5×10^{18} cm^{-3} positive charge density. In the absence of other charges and gates this charge pins the conduction band of InSb at about −0.069 eV below the Fermi level at the surface. For the InSb–Al interface we assume the conduction band of InSb is pinned −0.08 eV below the Fermi level due to the work function difference between the two materials. A negative band offset of the semiconductor to the superconductor is required for a hard induced gap in the InAs–Al system [21], and we assume a similar situation in InSb–Al hybrid devices. While the precise numbers for the surface accumulation and band-offset at the InSb–Al interface are unknown, it is known that InSb wires have about a 10 times smaller density than InAs wires [19, 53], and the parameters were adjusted from the InAs ones accordingly. The Al layer is assumed to be grounded, and enters as a Dirichlet boundary condition which is set to +0.08 V. The boundary condition at the substrate-dielectric interface is set to the applied gate voltage, V_{Gate}. On the remaining three boundaries of the system we use Neumann conditions. For the dielectric constant of InSb, the sputtered SiN_x, and the LPCVD Si_3N_4 we take take 15.15, 7.5, and 8, respectively.

After the electrostatic potential has been calculated for a given V_{Gate}, we plug it into the Schrödinger equation and solve it for the cross-section of the device. We use a Rashba Hamiltonian with a BdG superconducting term [56]

$$\begin{aligned} H = &\frac{\hbar^2}{2m^*(y,z)}(k_x^2 + k_y^2 + k_z^2)\tau_z - (E_F(y,z) + e\phi(y,z))\tau_z + \alpha_y(y,z)(k_z\sigma_x - k_x\sigma_z)\tau_z \\ &+ \alpha_z(y,z)(k_x\sigma_y - k_y\sigma_x)\tau_z + \frac{1}{2}g(y,z)\mu_B B\sigma_x + \Delta(y,z)\tau_x, \end{aligned} \tag{C.5}$$

where the effective mass m^*, the Fermi level E_F, the electrostatic potential ϕ, the Rashba parameters α_i, the g-factor and the superconducting pairing Δ are functions of the (y, z)-coordinates and depend on the material. Since ϕ is not solved in Al it is correspondingly set to zero there. The material parameters for InSb and Al are summarized in table C1. If desired, the orbital effect is added to equation (C.5) by the Peierls substitution $k_z \to k_z - \frac{\pi}{\phi_0}B(y - y_0)$, with ϕ_0 the magnetic flux quantum. y_0 is chosen such that the average vector potential in Al is zero, resulting in a vanishing supercurrent [24]. The Hamiltonian is discretised on a quadratic mesh and constructed using the `kwant` package [25]. To accommodate the small Fermi wavelength of Al a discretisation length of 0.1 nm is used.

Appendix D. Electric field dependence of spin–orbit coupling

The Rashba couplings α_y and α_z, which are nonzero only in the semiconductor region, result from the symmetry breaking by the electrostatic potential and are obtained from [52]

$$\alpha_i = \frac{eP^2}{3}\left[\frac{1}{E_0} - \frac{1}{(E_0 + \Delta_0)^2}\right]\bar{\mathcal{E}}_i, \tag{D.1}$$

where the average electric field in direction i is obtained by averaging $\mathcal{E}_i$ over the whole semiconductor region. Parameters for bulk InSb are used [52]: the Kane matrix element $P = 0.9641$ eV nm, the bandgap $E_0 = 0.237$ eV, and the spin–orbit gap $\Delta_0 = 0.810$ eV. The resulting Rashba parameters α_i are plotted in figure D1(a).

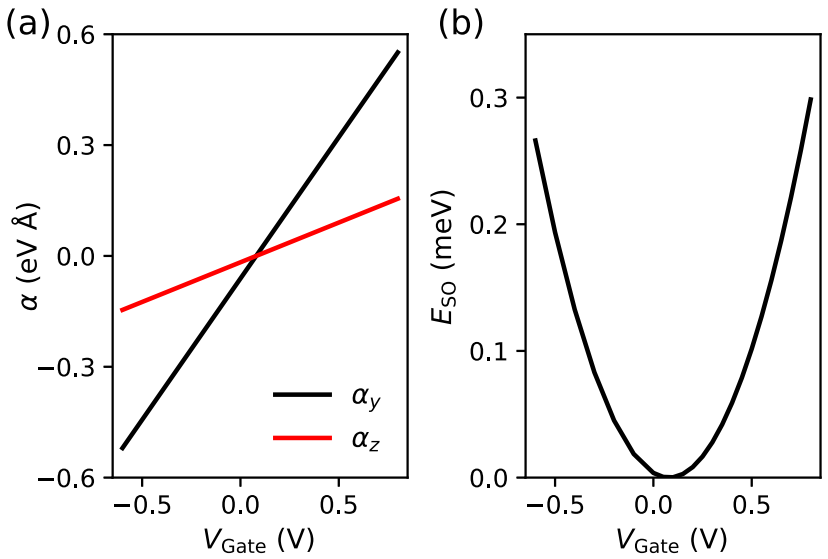

Figure D1. (**a**) Rashba coefficients α_y and α_z as a function of V_{Gate}. At $V_{\text{Gate}} = 0.08$ V, the average electric field in the wire goes to zero due to symmetry, leading to vanishing spin–orbit coupling. (b) Calculated E_{SO} as a function of V_{Gate}.

We define the spin–orbit energy $E_{\text{SO}} = \frac{m^*(\alpha_y^2 + \alpha_z^2)}{2\hbar^2}$. The spin–orbit energy is plotted as a function of V_{Gate} in figure D1(b). The average electric field in the nanowire increases as the applied gate voltage becomes more negative, leading to an enhancement of the spin–orbit coupling. At $V_{\text{Gate}} = 0.08$ V, the average electric field in the nanowire becomes equal to 0 due to symmetry, eliminating the influence of spin–orbit coupling on the nanowire spectrum.

Appendix E. Simulated band structure

The band structure of the superconductor-semiconductor nanowire system for different values of V_{Gate} is shown in figure E1. To quantify the coupling of a given state to the superconductor, we calculate the weight of the state in the semiconducting region SM (see figure 1(c)) as $W_{\text{SM}} = \iint_{\text{SM}} |\Psi(k_{\text{F}})|^2 \, \mathrm{d}y \, \mathrm{d}z$.

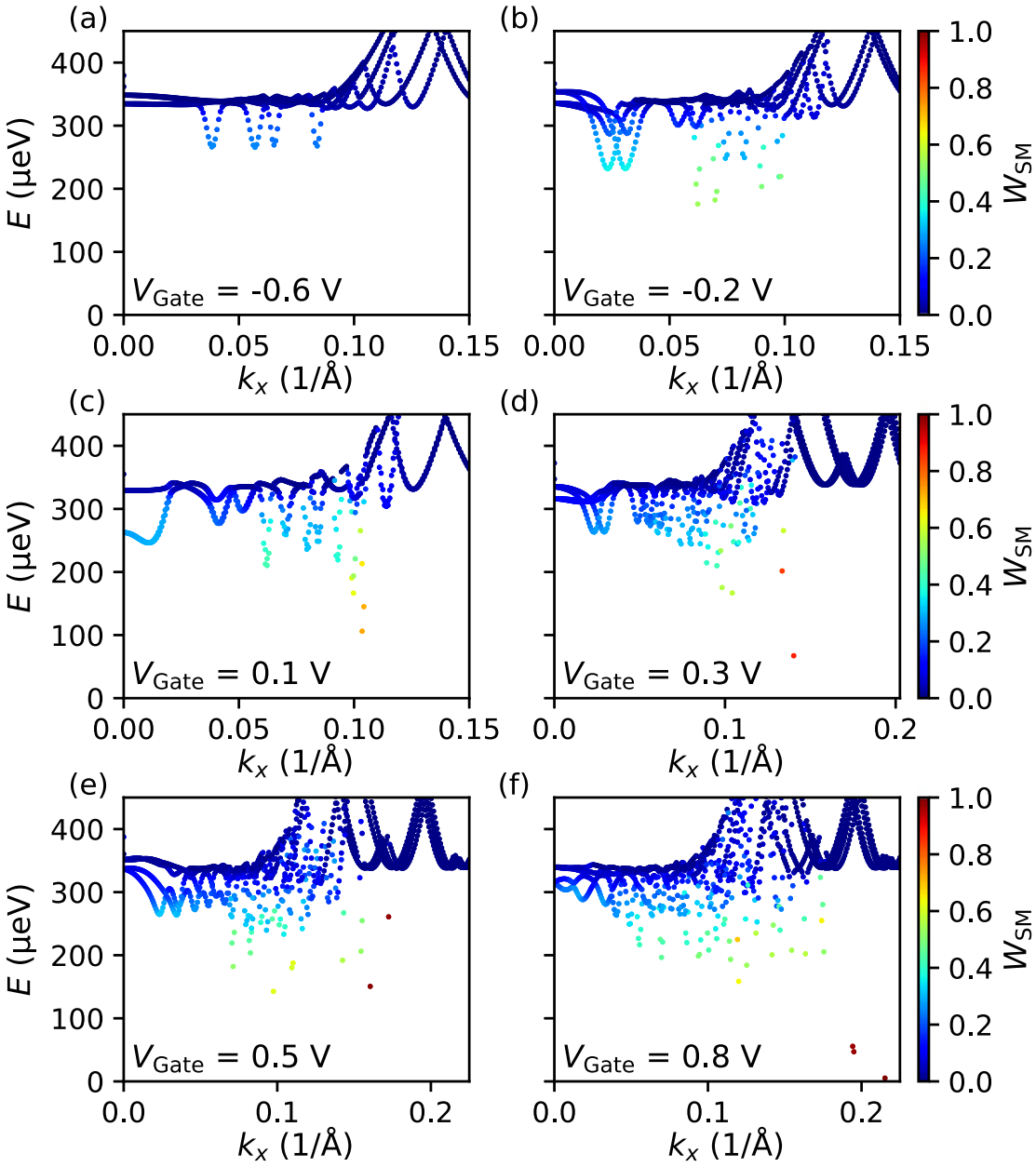

Figure E1. Band structure of the hybrid system calculated at $B = 0$ T for different values of V_{Gate}. The color indicates the weight of a given state in the semiconducting region. As the gate voltage is increased, the population of states with higher W_{SM} leads to a soft gap.

Appendix F. Gap fitting and additional data

To extract the gap, we measure the differential conductance dI/dV as a function of V_{Bias} and tunnel gate voltage V_{Tunnel} for different back gate voltages V_{BG}. In the tunneling limit, dI/dV is approximately proportional to the DOS. To ensure we are in this limit, we take only the traces where the conductance at high bias (~500 μV) is between 0.03 and 0.08 $\cdot$ $2e^2/h$. We use the BCS-Dynes expression for a dissipation broadened superconducting DOS [31] to arrive at the following expression for the conductance:

$$\frac{dI}{dV} = G_N \mathrm{Re}\left\{\frac{V_{Bias} - i\Gamma}{\sqrt{(V_{Bias} - i\Gamma)^2 - \Delta^2}}\right\}. \quad \text{(F.1)}$$

This equation is fitted to the data (separately for positive and negative bias), as shown in figure F1 for $V_{BG} = -0.6$ V. We take the average of the extracted gap values for different values of V_{Tunnel}, with the errorbar given by the standard deviation (results plotted in figure 2(e)).

Device B shows similar behavior to device A: as the side gate voltage is increased, the observed gap becomes smaller (as illustrated in figure F2).

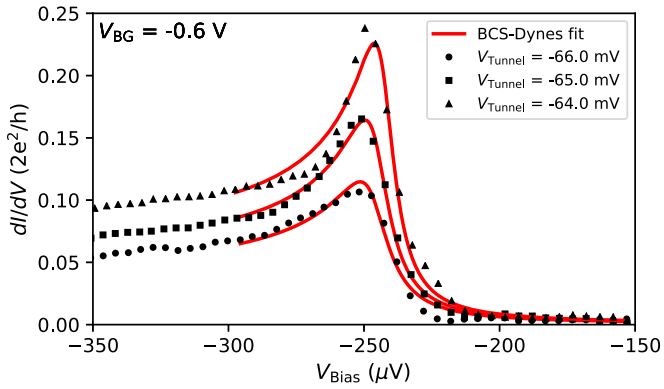

Figure F1. Fit (red line) of equation (F.1) to conductance data from device A (black circles, squares and triangles) for different values of the tunnel gate voltage.

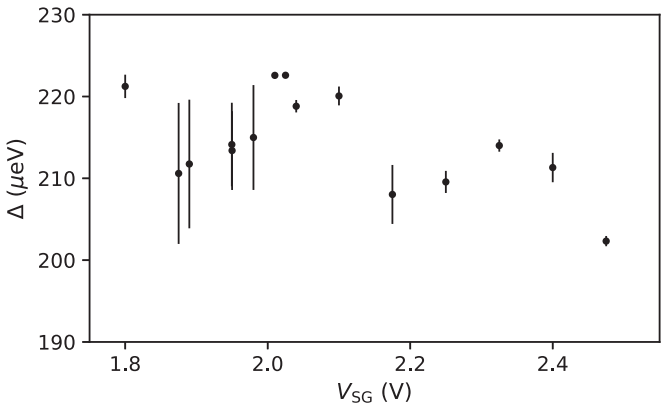

Figure F2. Extracted gap Δ as a function of V_{SG} for device B.

In figure F3, we show differential conductance traces as a function of V_{Bias} in device D for different values of the back gate voltage. The voltage on the tunnel gate is chosen such that the transmission through the junction (parameterized by G_N) is constant.

Although the sub-gap conductance is similar for all three gate voltages, there is a strong broadening of the coherence peak as the gate voltage becomes more positive. This broadening is associated with dissipation due to an increase in the number of quasiparticles, caused by pair breaking in the superconductor. We plot the extracted gap Δ and dissipation broadening Γ in figure F4.

As in the other devices, the gap decreases for more positive gate voltages, although in this case the effect is minor. The size of the gap is quite stable over an extended range in gate voltage. We speculate that this is related to the diameter of the wire, which is smaller than in the other devices. The reduced thickness means the superconductor can screen the gate voltage more effectively throughout the wire diameter, reducing the effect of the gate on the superconductor-semiconductor coupling.

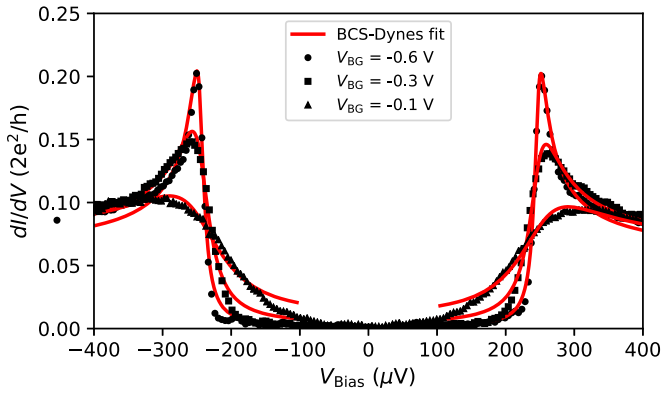

Figure F3. Fit (red line) of equation (F.1) to conductance data from device D (black circles, squares and triangles) for different V_{BG} at similar junction transparencies. The dissipation broadening sharply decreases for more negative gate voltages.

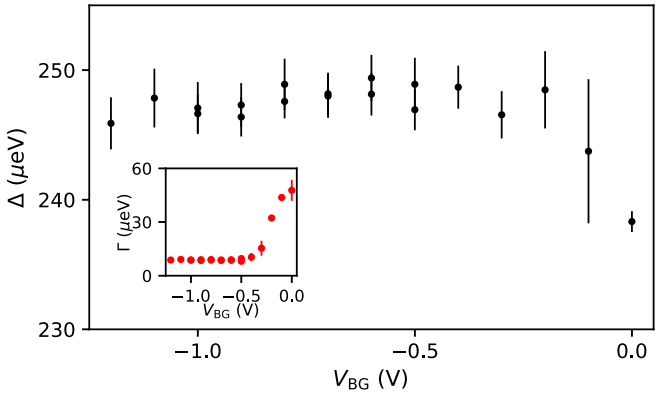

Figure F4. Extracted gap Δ as a function of V_{BG} for device D. Inset: dissipation broadening Γ as a function of V_{BG}. A decrease in the gap is accompanied by an increase in broadening, signaling the emergence of a soft gap.

Appendix G. *g*-factor fitting and additional data

For each back gate voltage, we measure the dI/dV as a function of V_{Bias} and the magnetic field B. We then identify the lowest energy peak in the spectrum. The position of this peak at a given field is obtained by a peak finding algorithm, the results of which are shown as the green circles in figure G1. The slope $\left|\frac{\Delta E}{\Delta B}\right|$ is determined by a linear fit (dashed black line in figure G1). From the slope, we get g_{eff} by using the relation $|\Delta E| = \frac{1}{2} g_{\text{eff}} \mu_B |\Delta B|$ for a spin-$\frac{1}{2}$ particle, with μ_B the Bohr magneton. This procedure is performed separately for positive and negative bias. The reported g_{eff} is then calculated as a weighted average of the absolute value of the positive and negative bias results (weights determined by the variance of the fit parameters).

The effective g-factor for device A is reported in the main text (figures 3(c) and 4(d), respectively). In figure G2, we plot the extracted g-factors of both L_1 and L_2 in device B. For completeness, data from device C is shown in figure G3.

The effective g-factor of L_1 (black circles) changes appreciately when the side gate voltage is changed, with the effect comparable to the one observed in device A. In contrast, g_{eff} of L_2 (red squares) is almost unaffected by the gate and has a lower value. This may be due to L_2 being closely confined near the superconductor, leading to a decreased g-factor due to stronger hybridization, and a weaker gate response due to enhanced screening.

To determine the importance of orbital effects, we calculate the nanowire spectrum as a function of magnetic field including this effect (figures G4(a), (b)). The orbital effect leads to an increase of the extracted values of g_{eff} and g_{spin} (figure G4(c)). Note that the definition of g_{spin} used in the main text is no longer valid when the orbital effect is included. Nevertheless, for consistency we apply the same procedure. As we do not observe these high g-factors in any of our devices, we conclude that the orbital effect does not give a significant contribution to the observed changes of g_{eff} with the gate voltage.

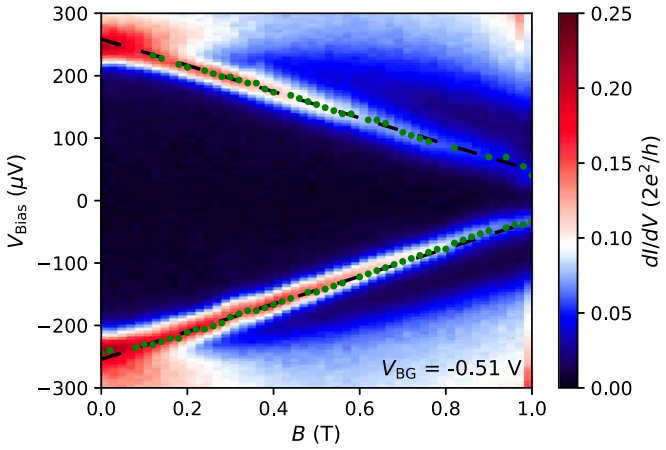

Figure G1. Differential conductance as a function of V_{Bias} and magnetic field. We apply a linear fit (dashed black lines) to the extracted peak positions (green circles) to obtain the average slope $|\frac{\Delta E}{\Delta B}|$.

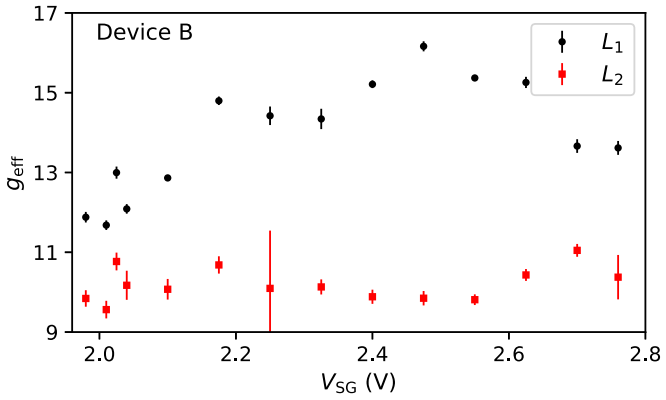

Figure G2. Extracted values of g_{eff} as a function of V_{SG} for L_1 (black circles) and L_2 (red squares) in device B.

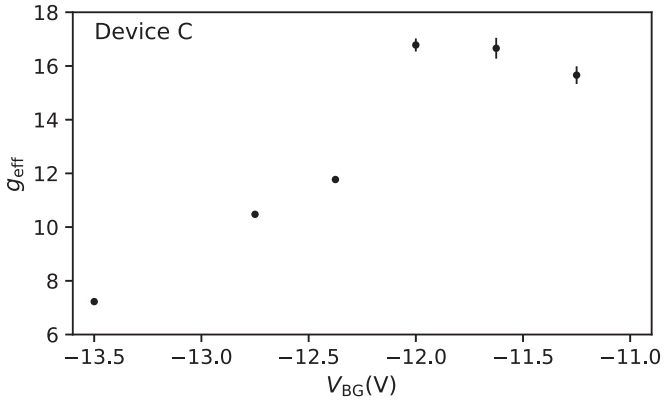

Figure G3. Extracted values of g_{eff} for device C.

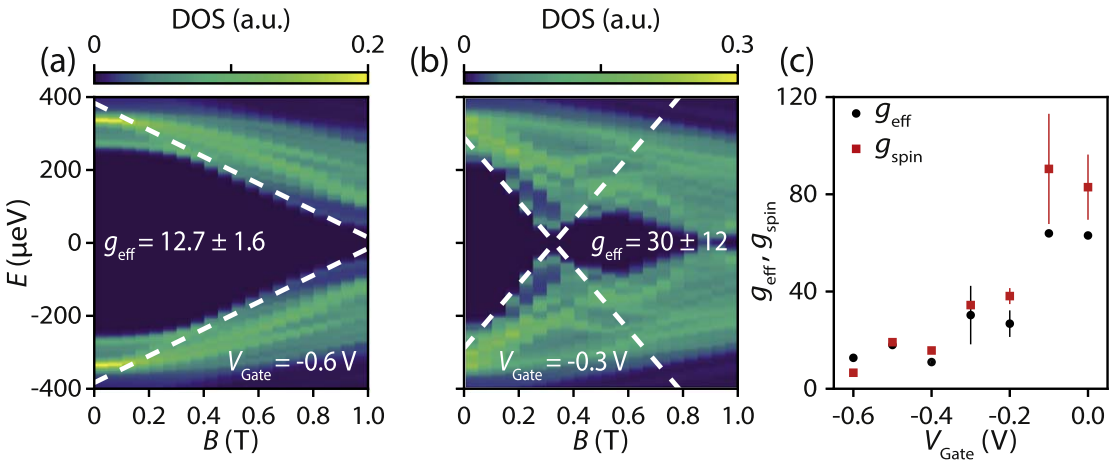

Figure G4. (a), (b) Simulated nanowire spectrum as a function of magnetic field including orbital effects. (c) Extracted g_{eff} (black circles) and g_{spin} (red squares) as a function of V_{Gate}.

Appendix H. Anticrossing fitting

Near the anticrossing, we approximate the energy of the lowest subgap state L_1 as $E_1 + \frac{1}{2}g_1\mu_{\mathrm{B}}B + aB^2$. The linear term represents the Zeeman contribution to the energy, while the quadratic term is a correction to account for the curvature at high fields. This is possibly due to the presence of additional levels interacting with L_1 in this field range. As the dispersion of L_2 is mostly linear in the field range of interest, we approximate it as $E_2 - \frac{1}{2}g_2\mu_{\mathrm{B}}B$. Adding the coupling parameter δ_{SO}, we find the energy levels of the coupled system from the eigenvalues of the matrix

$$\begin{bmatrix} E_1 + \frac{1}{2}g_1\mu_{\mathrm{B}}B + aB^2 & \delta_{\mathrm{SO}} \\ \delta_{\mathrm{SO}} & E_2 - \frac{1}{2}g_2\mu_{\mathrm{B}}B \end{bmatrix}.$$

By fitting the expression for the eigenvalues to the data (see figure H1), we extract the parameters $E_{1,2}$, $g_{1,2}$, a, and δ_{SO}. To prevent overfitting, we use estimates for the uncoupled asymptotes to constrain the fit parameters. From the obtained parameters we also calculate the splitting A, defined as the maximum deviation from zero energy of the lowest energy state L_1, after the first zero energy crossing has occurred.

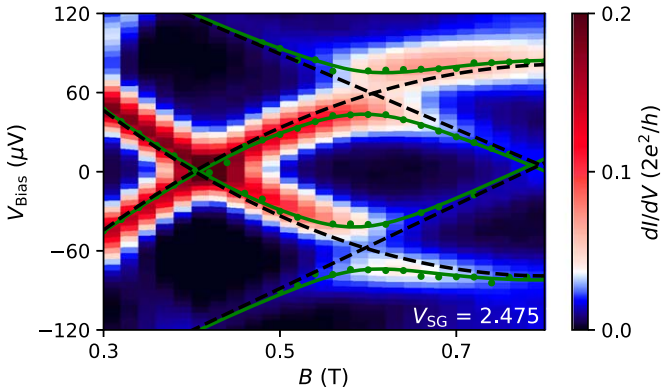

Figure H1. Data from device B, showing the differential conductance $\mathrm{d}I/\mathrm{d}V$ as a function of V_{Bias} and B for $V_{\mathrm{BG}} = 2.475$ V. Green dots indicate the peak positions found using a peak finding algorithm. The fit to the data is shown in green, with the uncoupled asymptotes as the black dashed lines.

Appendix I. Simulation of finite size nanowire system

To simulate the finite nanowire system, we solve the Hamiltonian (1) in a simplified setup. We consider a rectangular cross-section in the yz-plane similar to the one used in reference [21], where the top facet of the rectangle is covered by the superconductor, and a uniform gate voltage V_{Gate} is applied to the bottom facet, as illustrated in figure I1. First, we assume an infinitely long nanowire oriented in the x-direction, and calculate the electrostatic potential in the Thomas–Fermi approximation, similar to the procedure described in appendix C. The Fermi level in the nanowire is tuned such that it supports the same number of transverse modes at $V_{\mathrm{Gate}} = 0$ as the hexagonal nanowire studied previously. We use the same material parameters as in the previous simulation, which can be found in table C1.

We then plug the resulting electrostatic potential into (1) and solve the Schrödinger equation to find the low energy spectrum of the finite nanowire. We take a length of 750 nm, similar to the studied devices. We calculate only the modes in the semiconductor, assuming a superconducting gap of $\Delta = 250$ μeV. We find that the origin of the level repulsion between states is indeed spin–orbit coupling, which couples different longitudinal (along the x-direction) states within the same transverse (y- and z-directions) subband.

The result is illustrated in figure I2, where we plot the low energy spectrum as a function of Zeeman energy E_Z for a fixed value of V_{Gate} and different values of α. An increase in the spin–orbit coupling strength leads to an increase in the level repulsion.

However, even if α is fixed, the magnitude of the level repulsion can be changed by changing the confinement potential, as demonstrated in figure I3.

When the gate voltage is changed, it alters the confinement potential. This affects the energy of the levels coupled by the spin–orbit coupling, and as such directly influences the magnitude of δ, even though the spin–orbit coupling strength itself is not changed appreciatively. In figure I4 we plot the calculated energy gap due to level repulsion, 2δ, and the maximum splitting from zero energy of the lowest energy state after the first zero crossing, A, as a function of V_{Gate}. The two parameters follow opposite trends, consistent with the experimental observation in figure 4(f).

However, the trend with gate voltage is opposite: δ increases with more positive gate voltage, whereas in the experiment it decreases. We note that the geometry used in this simulation is a simplified version of the one used in the experiment. The dependence of the confinement energy on gate voltage is strongly dependent on the geometry, which differs between the simulation and the experiment. It is therefore expected that the trend of δ with gate voltage is not universal, and requires the details of the systems to be very similar before comparisons can be made.

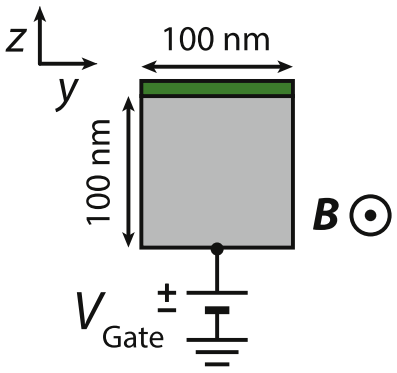

Figure I1. Schematic cross-section of the geometry used to simulate the finite nanowire system. A potential V_{Gate} is applied to the bottom facet, while the potential at the top facet is fixed by the work function difference between the two materials. The magnetic field is applied in the x-direction, along length of the nanowire.

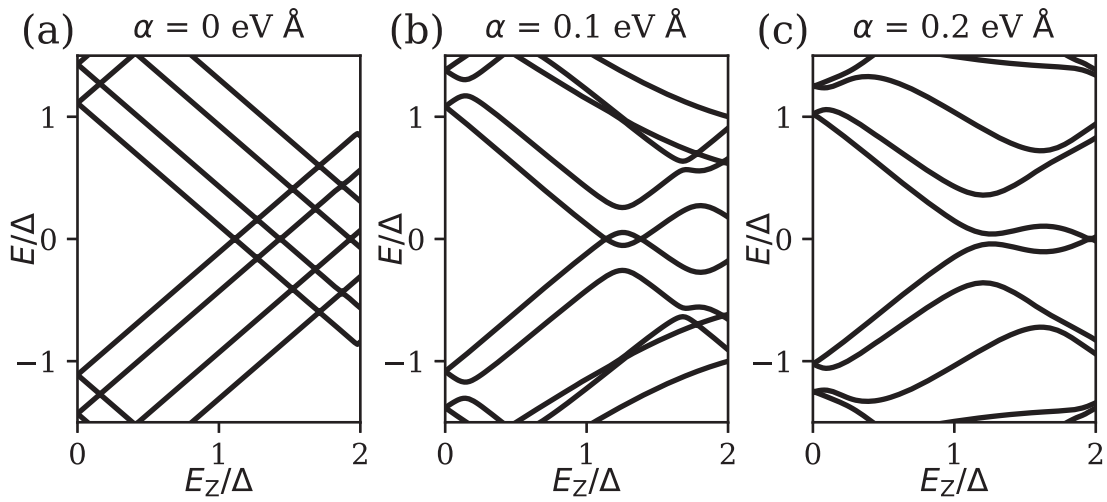

Figure I2. Calculated low energy spectrum of the finite size nanowire as a function of Zeeman energy for different values of α. Values calculated for $V_{\text{Gate}} = -0.536$ V, which is also used in main text figure 4(d). All energy scales are in units of the superconducting gap Δ.

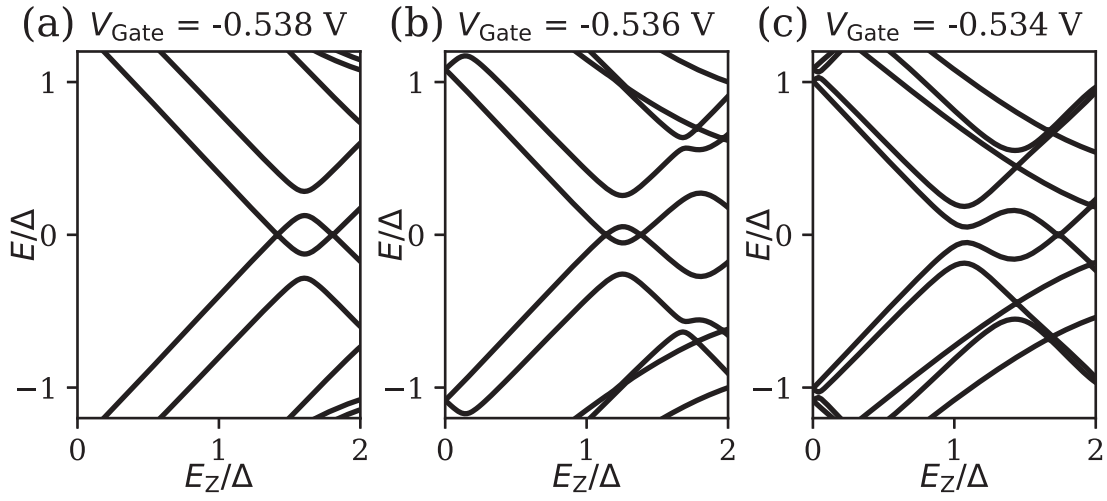

Figure I3. Calculated low energy spectrum of the finite size nanowire as a function of Zeeman energy for different values of V_{Gate}. Values calculated $\alpha = 0.1$ eV Å, energy scales in units of Δ.

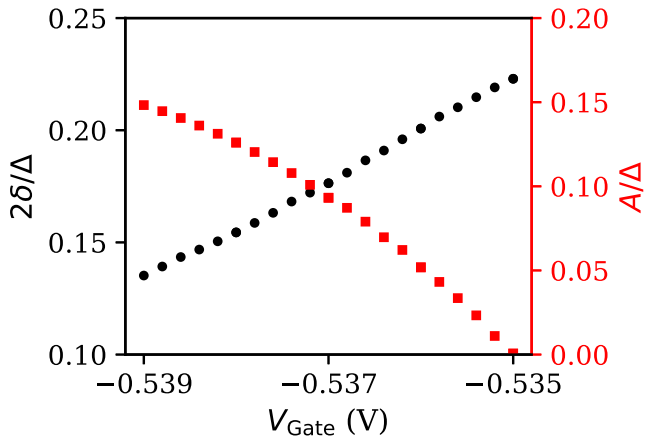

Figure I4. Dependence of the energy gap 2δ and the splitting A, in units of Δ, on the gate voltage V_{Gate}.

Appendix J. Additional ZBP data

Figure J1(a) shows the differential conductance measured in device A as a function of V_{Bias} and V_{Tunnel}, for $B = 0.35$ T and $V_{\text{BG}} = -0.37$ V. The low energy spectrum in this parameter regime does not depend on the transmission of the NS-junction. In figure J1(b), we show line traces for different values of V_{Tunnel}. Even though the transmission of the junction is changed by a factor of two, the peak position of the low energy states are not affected. Data from main text figure 5 was obtained for $V_{\text{Tunnel}} = -87$ mV.

Figure J2 shows additional data on the evolution of the level repulsion between L_1 and L_2 in device A (supplementing the data presented in main text figures 5(a)–(c)) as the back gate voltage is increased. As discussed in the main text, we do not find an extended region in parameter space with a stable zero bias conductance peak.

In figure J3 we show the low energy spectrum of device A as a function of V_{Bias} and V_{BG} for different magnetic fields (supplementing the data presented in main text figures 5(e), (f)). For specific combinations of magnetic field and gate voltage, we can find a zero energy state. However, as we do not find an extended region in parameter space, it is unlikely that a topological phase transition is responsible for this observation.

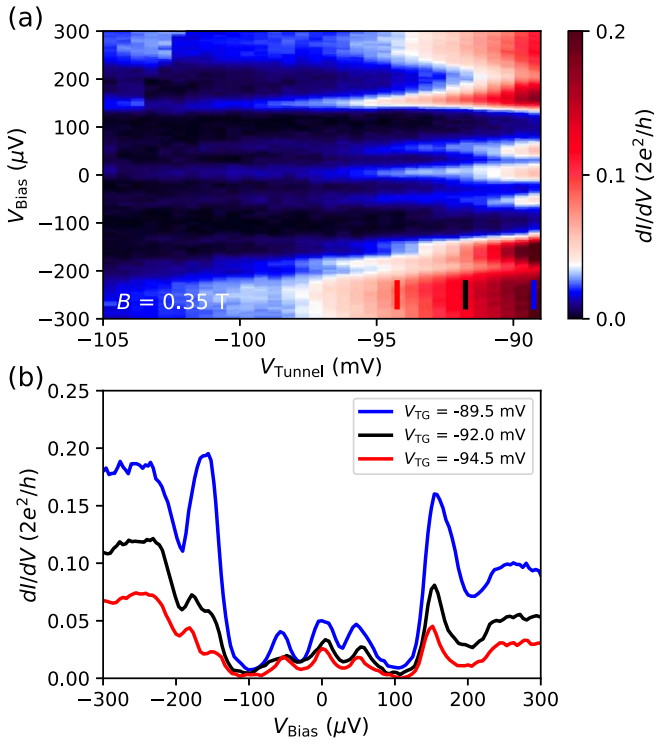

Figure J1. (**a**) $\mathrm{d}I/\mathrm{d}V$ measured in device A as a function of V_{Bias} and V_{Tunnel} for $B = 0.35$ T and $V_{\mathrm{BG}} = -0.37$ V. (b) Line traces at the values of V_{Tunnel} indicated by the colored lines in panel (a).

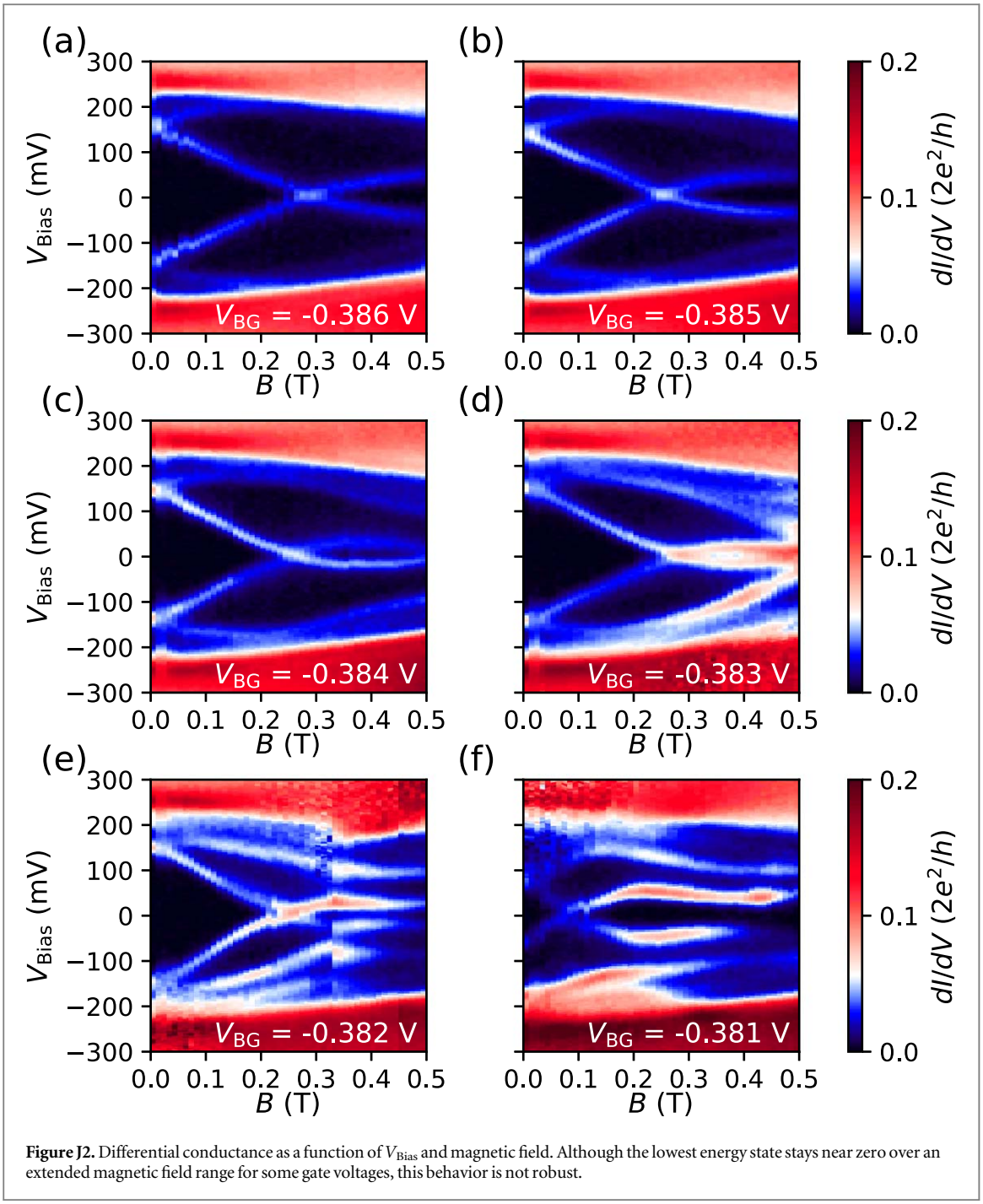

Figure J2. Differential conductance as a function of V_{Bias} and magnetic field. Although the lowest energy state stays near zero over an extended magnetic field range for some gate voltages, this behavior is not robust.

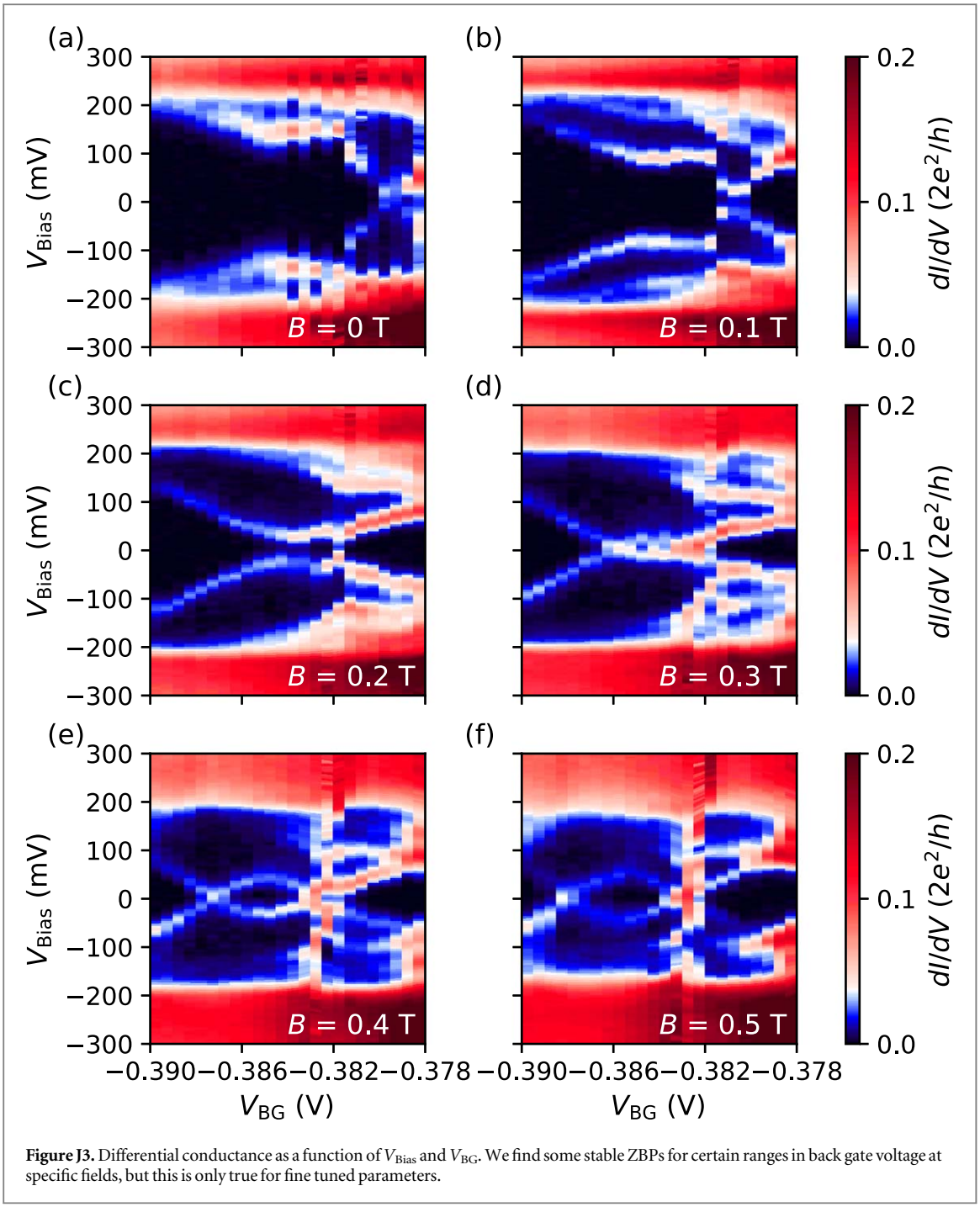

Figure J3. Differential conductance as a function of V_{Bias} and V_{BG}. We find some stable ZBPs for certain ranges in back gate voltage at specific fields, but this is only true for fine tuned parameters.

ORCID iDs

Di Xu https://orcid.org/0000-0002-7158-1469
Mihir Pendharkar https://orcid.org/0000-0003-1857-6131
Hao Zhang https://orcid.org/0000-0003-1734-6051

References

[1] Nayak C, Simon S H, Stern A, Freedman M and Das Sarma S 2008 *Rev. Mod. Phys.* **80** 1083
[2] Plugge S, Rasmussen A, Egger R and Flensberg K 2017 *New J. Phys.* **19** 012001
[3] Karzig T *et al* 2017 *Phys. Rev.* B **95** 235305
[4] Lutchyn R M, Sau J D and Das Sarma S 2010 *Phys. Rev. Lett.* **105** 077001
[5] Oreg Y, Refael G and von Oppen F 2010 *Phys. Rev. Lett.* **105** 177002
[6] de Gennes P G 1964 *Rev. Mod. Phys.* **36** 225
[7] Mourik V, Zuo K, Frolov S M, Plissard S R, Bakkers E P A M and Kouwenhoven L P 2012 *Science* **336** 1003

[8] Das A, Ronen Y, Most Y, Oreg Y, Heiblum M and Shtrikman H 2012 *Nat. Phys.* **8** 887
[9] Deng M T, Yu C L, Huang G Y, Larsson M, Caroff P and Xu H Q 2012 *Nano Lett.* **12** 6414
[10] Churchill H O H, Fatemi V, Grove-Rasmussen K, Deng M T, Caroff P, Xu H Q and Marcus C M 2013 *Phys. Rev.* B **87** 241401
[11] Gül O *et al* 2018 *Nat. Nanotechnol.* **13** 192
[12] Deng M T, Vaitiekėnas S, Hansen E B, Danon J, Leijnse M, Flensberg K, Nygård J, Krogstrup P and Marcus C M 2016 *Science* **354** 1557
[13] Zhang H *et al* 2018 *Nature* **556** 74
[14] Lutchyn R M, Bakkkers E P A M, Kouwenhoven L P, Krogstrup P, Marcus C M and Oreg Y 2018 *Nat. Rev. Mater.* **3** 52
[15] Gül O *et al* 2017 *Nano Lett.* **17** 2690
[16] Zhang H *et al* 2017 *Nat. Commun.* **8** 16025
[17] Gill S T, Damasco J, Janicek B E, Durkin M S, Humbert V, Gazibegovic S, Car D, Bakkers E P A M, Huang P Y and Mason N 2018 *Nano Lett.* **18** 6121
[18] Krogstrup P, Ziino N L B, Chang W, Albrecht S M, Madsen M H, Johnson E, Nygård J, Marcus C M and Jespersen T S 2015 *Nat. Mater.* **14** 400
[19] Chang W, Albrecht S M, Jespersen T S, Kuemmeth F, Krogstrup P, Nygård J and Marcus C M 2015 *Nat. Nanotechnol.* **10** 232
[20] Gazibegovic S *et al* 2017 *Nature* **548** 434
[21] Antipov A E, Bargerbos A, Winkler G W, Bauer B, Rossi E and Lutchyn R M 2018 *Phys. Rev.* X **8** 031041
[22] Volkov A F, Magnée P H C, van Wees B J and Klapwijk T M 1995 *Physica* C **42** 261
[23] Reeg C, Loss D and Klinovaja J 2018 *Phys. Rev.* B **97** 165425
[24] Nijholt B and Akhmerov A R 2016 *Phys. Rev.* B **93** 235434
[25] Groth C W, Wimmer M, Akhmerov A R and Waintal X 2014 *New J. Phys.* **16** 063065
[26] Vuik A, Eeltink D, Akhmerov A R and Wimmer M 2016 *New J. Phys.* **18** 033013
[27] Mikkelsen A E G, Kotetes P, Krogstrup P and Flensberg K 2018 *Phys. Rev.* X **8** 031040
[28] Bardeen J 1961 *Phys. Rev. Lett.* **6** 57
[29] Blonder G E, Tinkham M and Klapwijk T M 1982 *Phys. Rev.* B **25** 4515
[30] Beenakker C W J 1992 *Phys. Rev.* B **46** 12841
[31] Dynes R C, Narayanamurti V and Garno J P 1978 *Phys. Rev. Lett.* **41** 1509
[32] Winkler G W, Varjas D, Skolasinski R, Soluyanov A A, Troyer M and Wimmer M 2017 *Phys. Rev. Lett.* **119** 037701
[33] Stanescu T D, Lutchyn R M and Sarma S Das 2011 *Phys. Rev.* B **84** 144522
[34] Vaitiekėnas S, Deng M-T, Nygård J, Krogstrup P and Marcus C M 2018 *Phys. Rev. Lett.* **121** 037703
[35] Kammhuber J *et al* 2016 *Nano Lett.* **16** 3482
[36] Nitta J, Akazaki T, Takayanagi H and Enoki T 1997 *Phys. Rev. Lett.* **78** 1335
[37] van Weperen I, Tarasinski B, Eeltink D, Pribiag V S, Plissard S R, Bakkers E P A M, Kouwenhoven L P and Wimmer M 2015 *Phys. Rev.* B **91** 201413
[38] Scherübl Z, Fülöp G, Madsen M H, Nygård J and Csonka S 2016 *Phys. Rev.* B **94** 035444
[39] Stanescu T D, Lutchyn R M and Das Sarma S 2013 *Phys. Rev.* B **87** 094518
[40] Lee E J H, Jiang X, Houzet M, Aguado R, Lieber C M and Franceschi S De 2014 *Nat. Nanotechnol.* **9** 79
[41] van Heck B, Väyrynen J I and Glazman L I 2017 *Phys. Rev.* B **96** 075404
[42] O'Farrell E C T *et al* 2018 arXiv:1804.09676
[43] Pikulin D I, Dahlhaus J P, Wimmer M, Schomerus H and Beenakker C W J 2012 *New J. Phys.* **14** 125011
[44] Mi S, Pikulin D I, Marciani M and Beenakker C W J 2014 *J. Exp. Theor. Phys.* **119** 1018
[45] Mishmash R V, Aasen D, Higginbotham A P and Alicea J 2016 *Phys. Rev.* B **93** 245404
[46] Albrecht S M, Higginbotham A P, Madsen M, Kuemmeth F, Jespersen T S, Nygård J, Krogstrup P and Marcus C M 2016 *Nature* **531** 206
[47] Nadj-Perge S, Pribiag V S, van den Berg J W G, Zuo K, Plissard S R, Bakkers E P A M, Frolov S M and Kouwenhoven L P 2012 *Phys. Rev. Lett.* **108** 166801
[48] Sau J D, Tewari S and Das Sarma S 2012 *Phys. Rev.* B **85** 064512
[49] Kells G, Meidan D and Brouwer P W 2012 *Phys. Rev.* B **86** 100503
[50] Prada E, San-Jose P and Aguado R 2012 *Phys. Rev.* B **86** 180503
[51] Liu C-X, Sau J D, Stanescu T D and Das Sarma S 2017 *Phys. Rev.* B **96** 075161
[52] Winkler R, Papadakis S J, De Poortere E P and Shayegan M 2003 *Spin–Orbit Coupling in Two-Dimensional Electron and Hole Systems* vol 41 (Berlin: Springer)
[53] Plissard S R *et al* 2013 *Nat. Nanotechnol.* **8** 859
[54] Meservey R and Tedrow P M 1971 *J. Appl. Phys.* **42** 51
[55] Ashcroft N and Mermin N 1976 *Solid State Physics* (Philadelphia, PA: Saunders)
[56] Tinkham M 1996 *Introduction to Superconductivity* (*Dover Books on Physics Series*) (New York: Dover)